Anisotropic modelling of Opalinus Clay behaviour: from triaxial tests to gallery excavation application

François Bertrand[a,b], Frédéric Collin[a]

[a]Université de Liège, Département ArGEnCo / Géomécanique, Allée de la découverte 9, 4000 Liège, Belgium
[b]F.R.I.A, Fonds de la Recherche Scientifique - FNRS, Brussels, Belgium

Abstract

Deep repository in geological formations is the preferential solution considered by many countries to manage high-level nuclear wastes. In Switzerland, the Opalinus Clay is a candidate host rock. In this context, *in situ* and laboratory tests are conducted on Opalinus Clay to demonstrate the feasibility of deep disposal in this argillaceous formation. This paper presents a constitutive model able to fit the experimental data obtained from some triaxial tests conducted by Jahns [1] on cores from bore hole Schlattingen SLA-1. The elasto-plastic behaviour of Opalinus Clay is reproduced thanks to a Drucker-Prager model, taking into account the anisotropy behaviour of this sedimentary rock. The objective is to employ a single set of parameters representative of the material. In a second version of the model, the stress-dependency of the elastic properties and damage are taken into account. Finally, the parameters calibrated with experimental tests are used to simulate the excavation of a gallery with a second gradient approach.

Keywords: Opalinus Clay, Schlattingen, Constitutive Modelling, Anisotropy, Dilatancy, Localisation, tunnel Excavation

1. Introduction

Nuclear energy is widely used for electricity production all over the world [2]. Unfortunately, the nuclear fission process generates radioactive wastes that are hazardous to most forms of life. In the framework of long-term management of the high-level and high-lived radioactive wastes, a deep disposal in geological formations is envisaged as a long-term solution [3, 4]. Depending on their underground, different low-permeability host materials such as argillaceous, granite or salt formations are envisaged by the different radioactive waste management national agencies [5, 6]. In Switzerland, the Opalinus Clay is favoured by the NAGRA[1].

The Opalinus Clay is a sedimentary rock that has been deposited 180Ma ago and as many rocks, it is an anisotropic material. Its name is derived from a particular ammonite, the Leioceras opalinum, which is typical of the formation [7]. This clay has favourable properties for the deep geological disposal of radioactive wastes, a very low permeability but also an ability to self-seal [8]. The properties of Opalinus Clay are studied in a research facility near St-Ursanne in the Canton of Jura, it is the Mont Terri rock laboratory[2]. The Mont Terri project aims to demonstrate the feasibility of disposal in Opalinus Clay. In order to study the long term behaviour of the formation, numerical simulations are also employed. However, the experiments remain critical to deduce parameters employed by any model [9, 10, 11].

Recently, a combined finite-discrete element method (FEM/DEM) has been employed to represent the Opalinus Clay

behaviour [12]. Earlier, a special constitutive law was adopted by Gens [11] for the description of the stress-strain behaviour of Opalinus Clay: the material is considered as a composite made of the clay matrix, bonds and void spaces. The model includes degradation of bonding by damage. This kind of model requires a constitutive model for the matrix, a constitutive model for the bonds, and a stress-partitioning criterion to specify the way in which the applied stresses are shared.

This article focuses on the numerical modelling of some laboratory tests performed on Opalinus Clay samples taken from a well drilled at Schlattingen. The main objective of this study is to develop a hydro-mechanical model taking into account the anisotropic behaviour of the material and using a unique set of parameters to best fit the experimental data obtained from the laboratory tests. Numerical simulations on experimental tests aim to deduce missing constitutive parameters through back analysis. Then, with a representative set of parameters for the material, numerical simulations are employed for a predictive purpose. For example, the excavation of a tunnel can be simulated to model the excavation damaged zone (EDZ) [13].

The experiments data used in the present study are briefly described in section 2. The general framework is the elasto-plasticity, and anisotropy is both included on the elastic and plastic characteristics. The model is presented in section 3 and numerical results of some triaxial tests are presented in section 4. The model is then improved through different considerations in section 5. Actually, the loading of Opalinus Clay induces strain localisation that disrupts homogeneity of the material. In section 6, the strain localisation during a 2D plane strain biaxial test is modelled using a coupled local second gradient model. Finally, the excavation of a tunnel is simulated in section 7 with the parameters determined from the triaxial tests. This last sim-

---

[1]Nationale Genossenschaft für die Lagerung radioaktiver Abfälle, http://www.nagra.ch/en
[2]http://www.mont-terri.ch/

ulation also represents the appearance of strain localisation in shear band mode to model fractures.
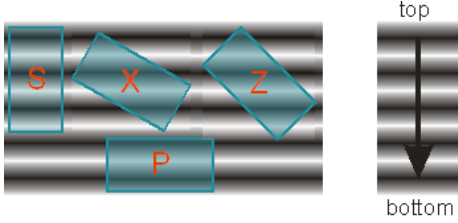
2. Experiments

Figure 1: Samples orientation with respect to bedding (horizontal lines) from [1].

Gesteinslabor Jahns [1] conducted uniaxial and triaxial compression tests on core samples of Opalinus Clay taken from the geothermal well of Schlattingen SLA-1 in the Molasse Basin of Northeastern Switzerland. These tests were performed along 4 anisotropy orientations, presented in Figure 1 and defined as:

- P-samples, parallel to bedding (0°)

- X-samples, oriented at 30° to bedding

- Z-samples, oriented at 45° to bedding

- S-samples, perpendicular to bedding (90°)

Sample		Diameter [mm]	Height [mm]	Volumetric mass [kg/m^3]
P115	(7.61 MPa)	25.46	50.65	2530
P109	(12.61 MPa)	25.37	49.45	2510
P13	(22.61 MPa)	25.37	50.70	2530
S106	(7.61 MPa)	25.49	50.53	2550
S106	(22.61 MPa)	25.47	49.88	2550
Z19	(7.61 MPa)	25.43	50.69	2550
Z23	(22.61 MPa)	25.46	50.80	2540

Table 1: Geometrical characteristics of samples considered.

A constant strain rate with a typical magnitude of 10^{-6} s^{-1} was followed. Only a limited number of triaxial compression tests were conducted at strain rates between 10^{-4} s^{-1} and 10^{-7} s^{-1} to investigate the effect of loading rate. Eleven uniaxial compression tests (Unconfined Compressive Strength, UCS tests) were performed under drained conditions while 13 triaxial compression tests were carried out under undrained conditions (after consolidation phase under drained conditions). For the triaxial tests, different confining pressures were applied (7.61, 12.61 and 22.61 MPa) and the saturation of each test was checked by Skempton tests [14]. Jahns reported an incomplete saturation for some of the tests.

Figure 2 gathers triaxial tests performed under the same confinement pressure but for three different loading directions. It highlights the anisotropic behaviour of Opalinus Clay. Thence, the elastic and plastic parameters were estimated for each direction [15]. Moreover, the different slopes in the linear parts of
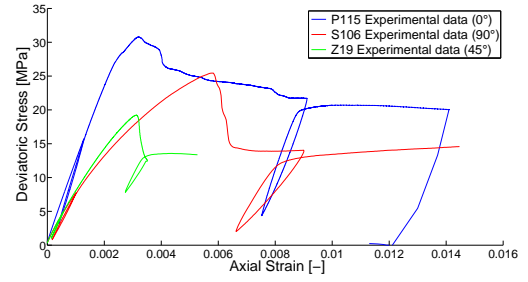

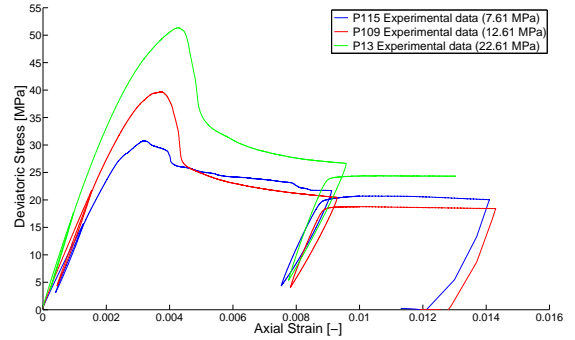Figure 2: Deviatoric Stress curves from triaxial tests under confinement pressure of 7.61 MPa.

Figure 3: P-sample tests (0°): Deviatoric Stress

the total stress-strain curves in Figure 3 suggest that the Young modulus also depends on the confinement pressure.

Experimental results show that the behaviour of Opalinus Clay is complex: the response is anisotropic, pressure and time dependent. In this study, we do not tackle the time dependency of the behaviour and we focus on the material response under the strain rate loading of 10^{-6} s^{-1}. Some of the triaxial tests are selected (Table 1) for numerical back analysis in order to identify the best parameter values for the Opalinus Clay. But first, the constitutive model used for the simulations is presented in the following section.

3. Constitutive model

The porous structure of the material is considered as superimposed continua [16]. The solid skeleton is formed by the assembly of grains and fluids fill the porous space. In this study, it is considered that water fully occupies the pores. Water mass balance and momentum balance equations are based on hydraulic and mechanical models presented below.

3.1. Balance equations

Water mass balance equation

Considering that the water is only in the liquid state, the water mass balance equation is written as:

$$\frac{\partial}{\partial t}(\rho_w n) + div(\rho_w \underline{q}_w) = Q_w \qquad (1)$$

where ρ_w $[kg/m^3]$ is the bulk density of water, n $[-]$ is the porosity, $\underline{q}_w$ $[m/s]$ is the mean velocity of the liquid phase and Q_w $[kg/(m^3 s)]$ is a source term.

Momentum balance equation

For quasi-static conditions, the momentum balance equation is:

$$div\,(\sigma_{ij}) = 0 \tag{2}$$

where σ_{ij} is the total stress tensor expressed by

$$\sigma_{ij} = \sigma'_{ij} - b_{ij}\,p_w\delta_{ij} \tag{3}$$

where b_{ij} is the Biot's coefficient and σ'_{ij} the effective stress tensor. For anisotropic porous materials, Biot coefficient is a tensor given by:

$$b_{ij} = \delta_{ij} - \frac{C_{ijkk}}{3K_s} \tag{4}$$

where δ_{ij} is the Kronecker symbol and K_s is the bulk modulus of the solid grains. For orthotropic elasticity, it reduces to a diagonal matrix. $b = 0.6$ is assumed as reference value for the Opalinus Clay [10]. This value is fixed for the orientations linked to the bedding plane. Depending on the elastic moduli, the third Biot coefficient is calculated to verify equation (4).

3.2. Hydraulic model
Darcy's law

The water advection is described by the Darcy law [17]. Neglecting the gravity effect, the Darcy fluid velocity $\underline{q}_w$ $[m/s]$ is a linear function of permeability and the gradient of water pressure $p_w [Pa]$:

$$\underline{q}_w = -\frac{k_{int}}{\mu_w}(\nabla p_w) \tag{5}$$

where μ_w $[Pa \cdot s]$ is the water dynamic viscosity and k_{int} $[m^2]$ is the material intrinsic permeability. In fact, considering hydraulic anisotropy, the permeability should be expressed as a tensor:

$$\underline{\underline{k}}_{int} = \begin{bmatrix} k_{xx} & k_{xy} & k_{xz} \\ k_{yx} & k_{yy} & k_{yz} \\ k_{zx} & k_{zy} & k_{zz} \end{bmatrix} \tag{6}$$

Equation (5) is valid under saturated conditions. The experimental tests are supposedly performed in these conditions. However, as a small portion of air is maybe present in the form of bubbles in the water phase, the water compressibility is adjusted.

Water specific mass

The water specific mass ρ_w $[kg/m^3]$ depends on pore water pressure:

$$\rho_w = \rho_{w0}\left[1 + \frac{p_w - p_{w0}}{\chi_w}\right] \tag{7}$$

where ρ_{w0} is the reference water specific mass at the reference pore water pressure p_{w0} and χ_w is the liquid compressibility coefficient.

3.3. Mechanical model

The general framework of the mechanical constitutive model is the elasto-plasticity. The elasto-plasticity principle consists of limiting the region of elastic deformation with a loading surface in the stress space. This concept allows splitting the total strain rate into elastic and plastic components:

$$\dot{\varepsilon}_{ij} = \dot{\varepsilon}^e_{ij} + \dot{\varepsilon}^p_{ij} \tag{8}$$

Elastic component

$\dot{\varepsilon}^e_{ij}$ is the ij strain rate component that does not modify the hardening state of the material; it is linked to the stress rate $\dot{\sigma}^e_{kl}$ through the Hooke's law:

$$\dot{\varepsilon}^e_{ij} = D^e_{ijkl} \cdot \dot{\sigma}^e_{kl} \tag{9}$$

where D^e_{ijkl} is the compliance matrix.

By inversing the matrix D^e_{ijkl} into C^e_{ijkl}, the elastic relation can also be written as:

$$\dot{\sigma}^e_{ij} = C^e_{ijkl} \cdot \dot{\varepsilon}^e_{kl} \tag{10}$$

For an isotropic material, the stiffness matrix depends only on two independent parameters, for example the Young modulus E and the Poisson's ratio ν. Dealing with anisotropic elasticity, until 21 independent parameters are required. However, the number of parameters is limited in many materials with axes of symmetry [18]. In the case where the anisotropy is induced by three orthogonal directions (*i.e.* orthotropy), the elastic matrix is defined with 9 parameters:

$$D^e_{ijkl} = \begin{bmatrix} \frac{1}{E_1} & -\frac{\nu_{21}}{E_2} & -\frac{\nu_{31}}{E_3} & 0 & 0 & 0 \\ -\frac{\nu_{12}}{E_1} & \frac{1}{E_2} & -\frac{\nu_{32}}{E_3} & 0 & 0 & 0 \\ -\frac{\nu_{13}}{E_1} & -\frac{\nu_{23}}{E_2} & \frac{1}{E_3} & 0 & 0 & 0 \\ 0 & 0 & 0 & \frac{1}{2G_{12}} & 0 & 0 \\ 0 & 0 & 0 & 0 & \frac{1}{2G_{13}} & 0 \\ 0 & 0 & 0 & 0 & 0 & \frac{1}{2G_{23}} \end{bmatrix} \tag{11}$$

The symmetry of the stiffness matrix imposes that:

$$\frac{\nu_{21}}{E_2} = \frac{\nu_{12}}{E_1} \quad ; \quad \frac{\nu_{31}}{E_3} = \frac{\nu_{13}}{E_1} \quad ; \quad \frac{\nu_{23}}{E_2} = \frac{\nu_{32}}{E_3}$$

In fact, sedimentary rocks such clays usually show a more limited form of anisotropy, the behaviour is isotropic in the bedding plane. This type of anisotropy is called cross-anisotropy or transverse isotropy [19]; it requires 5 independent parameters:

$$\begin{cases} E_1 = E_2 = & E_\parallel \\ E_3 = & E_\perp \\ \nu_{12} = \nu_{21} = & \nu_{\parallel,\parallel} \\ \nu_{13} = \nu_{23} = & \nu_{\parallel,\perp} \\ \nu_{31} = \nu_{32} = & \nu_{\perp,\parallel} \\ G_{13} = G_{23} = & G_{\parallel,\perp} \\ G_{12} = \dfrac{E_\parallel}{2(1+\nu_{\parallel,\parallel})} = & G_{\parallel,\parallel} \end{cases}$$

3

where subscripts ∥ and ⊥ refer respectively to the direction parallel to bedding (here directions 1 and 2) and perpendicular to bedding (direction 3).

Note that the axes of anisotropy do not necessarily coincide with the reference axes. In this more general situation, the relationship between the stress and the strain rates given by equation (9) is expressed only in the axes of orthotropy. Thence, transformations from one system to another are operated with rotation matrices. This aims at keeping the elastic matrix as simple as possible.

Plastic component

The plastic strain component in equation (8) can be expressed as the derivative of a plastic potential g:

$$\dot{\varepsilon}_{ij}^p = \dot{\lambda}^p \frac{\partial g}{\partial \sigma'_{ij}} \qquad (12)$$

where $\dot{\lambda}^p$ is the plastic multiplier.

The limit between the elastic and the plastic domain is represented by a yield surface f. The plastic multiplier is obtained from the consistency condition which rules that, during plastic flow, the stress state stays on the limit surface:

$$df \equiv \frac{\partial f}{\partial \sigma'_{ij}} \dot{\sigma}'_{ij} + \frac{\partial f}{\partial \kappa} \dot{\kappa} = 0 \qquad (13)$$

with κ the hardening variable.

It is proposed to reproduce the elasto-plastic behaviour of Opalinus Clay thanks to Drucker-Prager model [20]. As Mohr-Coulomb, it is an internal friction model suitable to simulate triaxial tests experiments.

The yield surface f is then given by the following equation:

$$f \equiv II_{\hat{\sigma}} + m \left(I_\sigma - \frac{3c}{\tan \phi} \right) = 0 \qquad (14)$$

where

- $I_\sigma = \sigma'_{ii}$ is the first invariant of the stresses.

- $II_{\hat{\sigma}} = \sqrt{\frac{1}{2} \hat{\sigma}'_{ij} \hat{\sigma}'_{ij}}$ is the second invariant of the deviatoric stresses.

- $\hat{\sigma}'_{ij} = \sigma'_{ij} - \frac{I_\sigma}{3} \delta_{ij}$ is the deviatoric stresses tensor.

- ϕ is the friction angle.

- c is the cohesion, depending on the bedding plane orientation. Indeed, as it is presented below, the anisotropy of the plastic behaviour is introduced through the cohesion.

- m is a coefficient function of friction angle as

$$m = \frac{2 \sin \phi}{\sqrt{3}(3 - \sin \phi)}$$

In the case of internal friction model, the plastic potential g is defined using a similar expression to the one of the loading surface:

$$g \equiv II_{\hat{\sigma}} + m' I_\sigma \qquad (15)$$

with $m' = \dfrac{2 \sin \psi}{\sqrt{3}(3 - \sin \psi)}$ and ψ the dilatancy angle.

The use of a hardening Drucker-Prager model allows hardening/softening processes during plastic flow. This is introduced via a hyperbolic variation of the friction angle and the cohesion between initial (ϕ_0 and c_0) and final (ϕ_f and c_f) values as a function of the Von Mises equivalent plastic strain ε_{eq}^p [21]:

$$\phi(\varepsilon_{eq}^p) = \phi_0 + \frac{(\phi_f - \Phi_0) \cdot \varepsilon_{eq}^p}{B_p + \varepsilon_{eq}^p} \qquad (16)$$

$$c(\varepsilon_{eq}^p) = c_0 + \frac{(c_f - c_0) \cdot \varepsilon_{eq}^p}{B_c + \varepsilon_{eq}^p} \qquad (17)$$

where the Von Mises equivalent plastic strain ε_{eq}^p is obtained by integration of the Von Mises equivalent plastic strain rate $\dot{\varepsilon}_{eq}^p$:

$$\varepsilon_{eq}^p = \int_0^t \dot{\varepsilon}_{eq}^p \qquad \text{with} \quad \dot{\varepsilon}_{eq}^p = \sqrt{\frac{2}{3} \dot{\hat{\varepsilon}}_{eq}^p \dot{\hat{\varepsilon}}_{eq}^p} \qquad (18)$$

Coefficients B_p and B_c represent respectively the values of equivalent plastic strain for which half of the hardening/softening on friction angle and cohesion is achieved (Figures 4 and 5).

In addition, a parameter δ can be used to create an offset between the time when starting the variation on the cohesion and the friction angle, *i.e.* between the softening and the hardening. Then, equation (17) becomes:

$$c(\varepsilon_{eq}^p) = c_0 + \frac{(c_f - c_0) \cdot (\varepsilon_{eq}^p - \delta)}{B_c + (\varepsilon_{eq}^p - \delta)} \qquad (19)$$

With this δ parameter, the half of the softening on cohesion is achieved for an equivalent plastic strain equal to $B_c + \delta$.
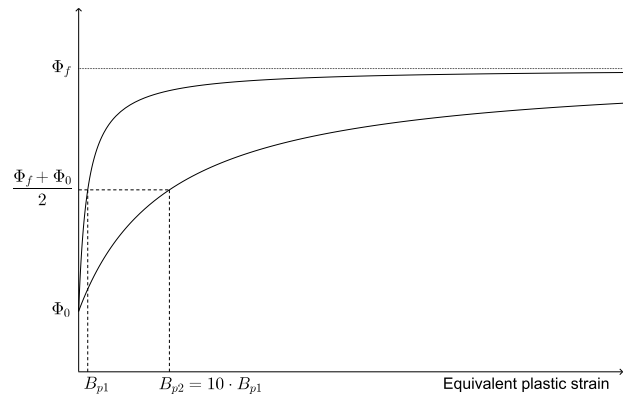

Figure 4: Hyperbolic evolution of friction angle with plastic strain

The anisotropic model assumes that the strength of materials varies according to the orientation of the principal compressive stress with respect to the bedding plane orientation. The
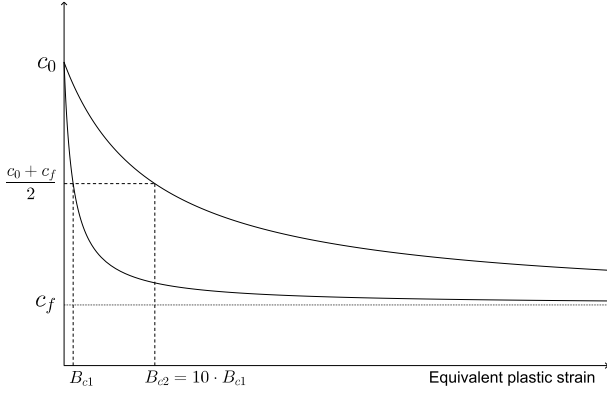
4

Figure 5: Hyperbolic evolution of cohesion with plastic strain

model used takes into account the anisotropy through the cohesion which depends on the angle between major principal stress and the normal to the bedding plane [22, 23].
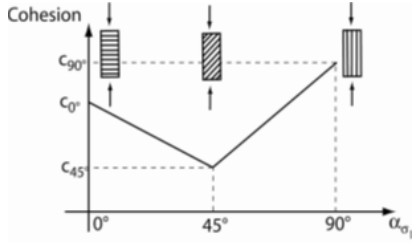

Figure 6: Schematic view of the cohesion evolution as a function of the angle between the normal vector to bedding plane and the direction of major principal stress.

Three cohesion values are defined: for major principal stress parallel ($\alpha_{\sigma_1} = 0°$), perpendicular ($\alpha_{\sigma_1} = 90°$) and with an angle of 45° ($\alpha_{\sigma_1} = 45°$) with respect to the normal to bedding plane. Between those values, cohesion varies linearly with α_{σ_1}. The mathematical expression of the cohesion is:

$$c = max\left[\left(\frac{c_{45°} - c_{0°}}{45°}\right) + c_{0°} ; \left(\frac{c_{45°} - c_{0°}}{45°}\right)(\alpha_{\sigma_1} - 45°) + c_{45°}\right]$$

with α_{σ_1} being the angle between the normal to the bedding plane $\vec{n}$ and the major principal stress $\vec{\sigma}'_1$.

This definition of the cohesion is proper for triaxial test conditions. For the a tunnel excavation, the orientation of the major principal stress is not constant. The cohesion is thus modified while the orientation of the bedding does not evolve. The model could be improved by directly link the cohesion to the orientation of the bedding with a microstructure fabric tensor [24, 25]. Moreover, there is a lack of data to take into account the Lode angle although the loading path followed is not pure compression during the excavation.

4. Triaxial tests simulations

The numerical code used for the simulations is the Finite Element code LAGAMINE. This code is born at the University

of Liege at the end of the 70's and has been developed along for the last forty years so that it constitutes a unique numerical tool for the THM-related modeling in the fields of underground nuclear waste storage, geothermal energy, oil and gas applications [26, 27].

In this study, triaxial tests are modelled as undrained 2D axisymmetric problems, the axis of the core sample ("y-axis") representing the radial symmetry axis. Furthermore, the symmetry plane through the centre of the core sample is applied to cut the model domain. According to Figure 7, roller boundary conditions are applied for the symmetry axis y and the symmetry plane y=0, whereas stresses are specified for all other boundaries. The geometrical characteristics of samples were given in Table 1. Only one coupled hydro-mechanical element is used.

Confining pressure is imposed by constant σ_3 loading and shearing phase by constant strain rate $\dot{\varepsilon} = 10^{-6} s^{-1}$. For all triaxial tests, temperature is assumed constant and equal to 24°C.
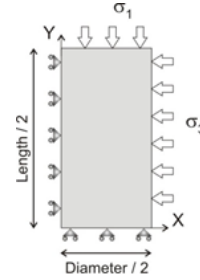

Figure 7: Schematic view and boundary conditions of triaxial problem of numerical model.

Some of triaxial tests are analysed numerically for different orientations with bedding (see Table 1 for the geometry of the samples):

- P115, P109 and P13 tests in P-samples orientation

- S106 and S102 in S-samples orientation

- Z19 and Z23 in Z-samples orientation

These tests correspond to three different confining pressures: 7.61, 12.61 and 22.61 MPa. First, these tests are calibrated to identify the best fitting for each direction assuming an isotropic elasto-plastic model (Drucker-Prager hardening plasticity model). The parameters of the simulations and the corresponding results are presented in Appendix A. We tried to use the same strength parameters for all the tests carried out in the same direction; it explains why some simulations deviate from the strength peak experimentally observed. The objective was to calibrate all samples from one direction together rather than calibrate all samples one by one. However, given the significant difference between the two S-samples tests, different friction angles were used for this direction with the isotropic model.

5

	$E_\parallel$	$E_\perp$	$\nu_{\parallel\parallel}$	$\nu_{\parallel\perp}$	ψ	ϕ'_0	ϕ'_f	B_p	c'_{init}	c'_{final}	B_c	δ	$\frac{1}{\chi}$
S102	18.7	9.5	0.22	0.34	-2.8°	18.75°	25°	1.0E-4	$c'_{0°} = 9.01$ $c'_{45°} = 3.74$ $c'_{90°} = 3.61$	$c'_{0°} = 9.01\text{E-5}$ $c'_{45°} = 3.74\text{E-5}$ $c'_{90°} = 3.61\text{E-5}$	0.002	0.0062	3.5E-9
S106	13.8	7.8										0.004	6.5E-9

Table 2: Orthotropic parameters; E [GPa], c' [MPa] and $\frac{1}{\chi}$ [Pa^{-1}].

As the objective is to determine a relevant set of parameters for the excavation of a tunnel, it is preferable to use only one anisotropic model with a single set of parameters. A set of parameters can be deduced from the isotropic analysis, as presented in Table 2. In fact, the 2D axisymmetric model requires an horizontal bedding plane and only data from the S-samples tests are therefore tested. A 3D-model is not developed since the tunnel excavation is studied with a 2D-plane calculation over its cross section. However, a 3D-model could serve to study all the 3D effects.

Figures 8 and 9 present the evolutions of the deviatoric stress and the pore pressure with the axial strain obtained with the orthotropic model for the S-samples. Experimental data and results of the simulations are compared. It can be observed in Table 2 that the same set of parameters is used except the Young moduli which are stress-dependent, the δ coefficient and the water compressibilities χ which are sample dependent. The fact that the water compressibility has to be modified between the tests is certainly linked to a water saturation that was not completely achieved for all the tests.
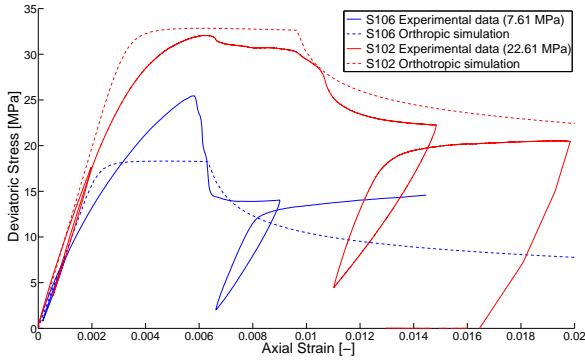

Figure 8: S-samples: Deviatoric Stress: Experimental curves and orthotropic simulations

Certainly, experimental data can be better represented with the isotropic model using individual parameters for each direction. But as we said, it is not the objective because the simulation of the excavation of a tunnel requires a single set of parameters.

In this perspective, we improve the model to account the dependency of the Young modulus to the confinement pressure. Morever, the pore pressure could be better represented by introducing a variable dilatancy angle. These improvements are
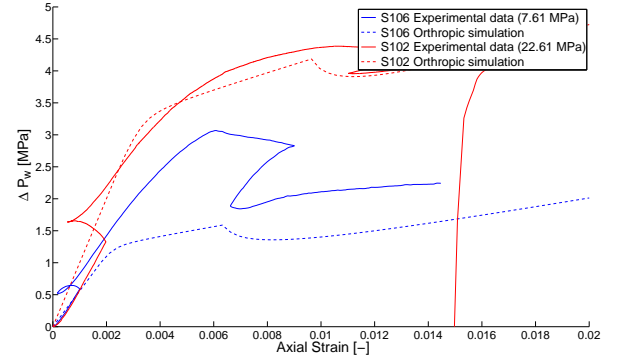

Figure 9: S-samples: Pore Pressure: Experimental curves and orthotropic simulations

considered in the following section.

5. Model improvements

We introduce a dependency of the elastic moduli to the mean stress but also to the damage. Then, a variation of dilatancy angle is implemented.

5.1. Stress-dependent elastic moduli

The experiments conducted on Opalinus clay have shown that the Young modulus is a function of the confinement pressure. It is a fact and it should be taken into account. Based on experimental data (Young moduli for different confinement pressures), interpolations can be determined [15].

For each direction, instead of one Young modulus, two parameters are used: the y-intercept (E_0) and the slope (α_E) of the linear evolution of the Young modulus with confinement. Then, the Young modulus is:

$$E = E_0 + \alpha_E \cdot |\sigma_M| \qquad (20)$$

in the case where σ_M is a compressive stress (negative in the Lagamine code). Otherwise, the y-intercept value is attributed to the Young modulus.

5.2. Evolution of elastic moduli with damage

The damage induced by microcracks is an important dissipation mechanism in the case of cohesive geomaterials. The damage affects the hydro-mechanical properties of the material and it is an important aspect in the context of tunnel excavation.

Indeed, the convergence of the tunnel is influenced by the excavation damaged zone (EDZ). The damage model is inspired from [28] and [29]. This model is formulated in the framework of thermodynamics.

The elastic stiffness tensor $\mathbf{C}$ of the damaged material is given by

$$\mathbf{C}(d) = (1 - d)\mathbf{C}^0 \tag{21}$$

with d the damage variable representing the density of microcracks and $\mathbf{C}^0$ the anisotropic elastic stiffness tensor of the undamaged material.

The phenomenon of damage is linked to the loading path and may be therefore anisotropic. However, it is assumed that the induced anisotropy is negligible compared with the initial structural anisotropy, the induced damage is therefore assumed isotropic and it is simply described by the scalar variable d.

The concept of damage effective stress (σ^*) is adopted. It consists of defining the stresses relative to the undamaged section.

$$\sigma^* = \frac{\sigma}{1 - d} \tag{22}$$

The damage evolution is derived by using a damage criterion:

$$F_d(Y_d, d) = Y_d - Y_d^0(1 + P \cdot d) \tag{23}$$

where Y_d is the thermodynamic force associated with the damage variable. Y_d^0 is the initial damage energy release threshold and P a parameter controlling damage evolution rate. For the sake of simplicity and in absence of more information, a linear function has been chosen for the damage criterion. It is the criterion proposed by [29] for argillite. Any other expression could be used by the model if data were available.

If $F_d \leqslant 0$, then the damage variable does not evolve.
But if $F_d > 0$, then

$$d = \frac{Y_d - Y_d^0}{P \cdot Y_d^0}$$

The damage variable is limited to a maximum value of 0.9.

The thermodynamic damage force Y_d is derived from a thermodynamic potential $\mathbf{\Psi}$ which can be expressed in the general form:

$$\mathbf{\Psi} = \frac{1}{2}(\varepsilon - \varepsilon^p) : \mathbf{C}(d) : (\varepsilon - \varepsilon^p) + \Psi_p(\varepsilon_{eq}^p, d) \tag{24}$$

where $\Psi_p(d, \varepsilon_{eq}^p)$ is the locked plastic energy for plastic hardening.

The thermodynamic force associated with the damage is then given by

$$\begin{aligned} Y_d &= -\frac{\partial \mathbf{\Psi}}{\partial d} \\ &= -\frac{1}{2}(\varepsilon - \varepsilon^p) : \mathbf{C}'(d) : (\varepsilon - \varepsilon^p) - \frac{\partial \Psi_p(\varepsilon_{eq}^p, d)}{\partial d} \end{aligned} \tag{25}$$

where $\mathbf{C}'(d)$ is the derivative of the elastic tensor with respect to damage variable. Given (21), we have

$$\mathbf{C}'(d) = \frac{\partial \mathbf{C}(d)}{\partial d} = -\mathbf{C}^0 \tag{26}$$

Then, assuming that the plastic hardening is independent of the damage $\left(\dfrac{\partial \Psi_p(\varepsilon_{eq}^p)}{\partial d} = 0 \right)$, equation (25) is reduced to

$$Y_d = \frac{1}{2}(\varepsilon - \varepsilon^p) : \mathbf{C}^0 : (\varepsilon - \varepsilon^p) \tag{27}$$

Actually, plastic deformation is generally coupled with damage due to growth of microcracks. Then, the induced damage is the main mechanism responsible of material softening. However, because plastic deformation is a dominant mechanism in the case of hard clay rocks [28], hardening and softening processes during plastic flow were already introduced in the first model. Indeed, the friction angle and the cohesion are function of the Von Mises equivalent plastic strain thanks to some hyperbolic variations between initial and final values (equations (16) and (19)).

Thence, only the elastic part is considered to derive the damage variable evolution. It is equivalent to consider there is no coupling between damage evolution and plastic flow. Thence, the damage variable increases in the elastic domain and after it stabilizes. Then, hardening and softening are controlled independently from the damage.

5.3. Variable dilatancy angle

Regarding the evolution of the pore pressure as a function of the axial deformation, it is evident that the dilatancy is not constant during the plastic loading. The behaviour is more contractant at the beginning of the plastic regime and becomes more dilatant as long as the loading is going on. The dilatancy angle should therefore not be constant in the model.

The following relationship defining the dilatancy angle as a hyperbolic function of the plastic deformations is proposed [30]:

$$\psi(\varepsilon_{eq}^p) = \psi_0 + \frac{(\psi_f - \psi_0) \cdot \varepsilon_{eq}^p}{B_d + \varepsilon_{eq}^p} \tag{28}$$

where ε_{eq}^p is the Von Mises equivalent plastic strain.

As shown in Figure 10, this relationship is an hyperbolic function. Thus, the same equations are used to describe the variation of the friction angle and the dilatancy angle.

ψ_0 and ψ_f are respectively the initial and the final values of the dilatancy angle. B_d represents the value of the equivalent plastic strain for which half of the evolution of the dilatancy angle is achieved.

5.4. Numerical results

The parameters taken for the improved orthotropic model are given in Table 3. The cohesions given in this Table correspond to the initial cohesions in three directions and r_c is the ratio between initial and final cohesions. One can observe that the

$E_{/\!/}$	$\alpha_{E_{/\!/}}$	$E_\perp$	$\alpha_{E_\perp}$	$\nu_{/\!//\!/}$	$\nu_{/\!/\perp}$	P	Y_d^0
10.41	0.5516	5.87	0.1852	0.22	0.34	600	0.002

ψ_0	ψ_f	B_d	ϕ'_0	ϕ'_f	B_p	$c'_{0°}$	$c'_{45°}$	$c'_{90°}$	r_c	B_c
-6.0°	2.0°	0.003	18.75°	25°	1.0E-4	9.01	3.56	3.70	1.0E+5	0.002

Table 3: Parameters for the improved orthotropic model; E [GPa], α_E for σ_M [MPa], c' [MPa], Y_d^0 [MPa].
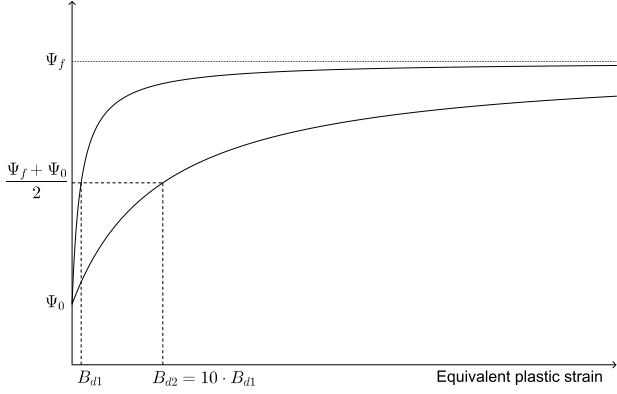
Figure 10: Hyperbolic evolution of dilatancy angle with plastic strain

same set of parameters can be therefore used for any confinement pressure.

Figure 11 presents the evolution of the deviatoric stress with the axial strain for the S-samples and Figure 12 the evolution of the pore pressure. Only the δ coefficient and the water compressibilities are sample dependent (Table 4).

	δ	$\dfrac{1}{\chi}$
S106	0.004	4.5E-9
S102	0.0062	3.5E-9

Table 4: Sample dependent parameters; $\frac{1}{\chi}$ [Pa^{-1}].

The improvement of numerical simulations does not seem really significant. In fact, the model improvements were mainly implemented to be in agreement with the experimental observations. First, the stress-dependency of the elastic moduli and then the evolution of these moduli with damage. Indeed, the experiments carried out on Opalinus clay showed on the first hand the Young modulus is a function of the confinement pressure and on the second hand the modulus determined during the unloading path is different from the initial loading path. Based on these facts, the model has been improved. The overall curve is not really improved because the dependency of the elastic moduli on the mean stress and the evolution of the parameters with damage have antagonistic effects on the deviatoric stress curve.

Nevertheless, the main advantage of the new model is the definition of only one set of parameters for any confinement pressure. A unique set of parameters can therefore be used for all the simulations. Indeed, one of the goals pursued was to find one set of parameters fitting as well as possible all the experimental tests rather than taking into account the experimental variability. Indeed, by defining different sets of parameters for the different experiments, the simulations could approximate perfectly the experimental curves.

Finally, the introduction of a variable dilatancy angle helps best fit the pore pressure evolution.
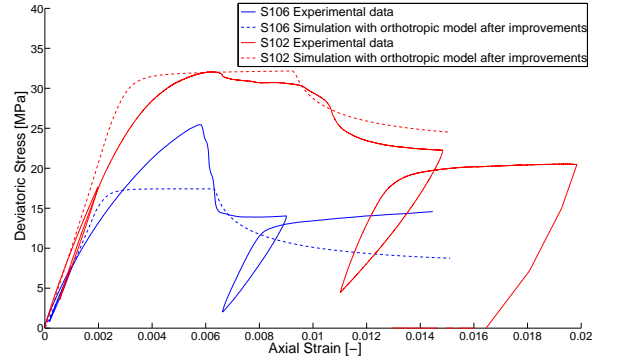

Figure 11: S-samples: Deviatoric Stress with the orthotropic model after improvements
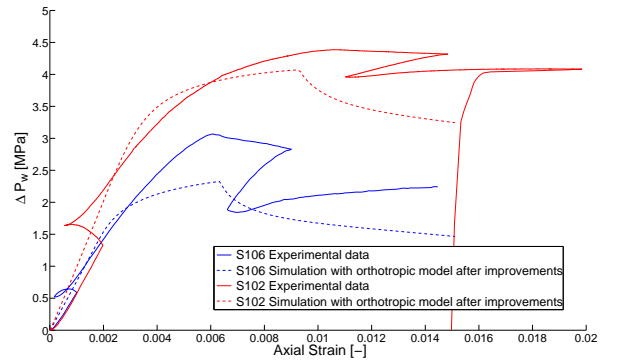

Figure 12: S-samples: Pore Pressure with the orthotropic model after improvements

The model used to obtain these numerical results assumes the material stays homogeneous. Actually, it is not the case because failure in the Opalinus Clay is often preceded by progressive strain localisation, leading finally to failure lines. In the

following section, the ability of the Lagamine code to model strain localisation in geomaterials is demonstrated with a 2D plane strain biaxial test.

6. Localised shear strain modelling

Starting from a homogeneous state, the strain localisation consists in the accumulation of strain in a limited zone, potentially leading to material damage. A coupled local second gradient model is used together with the cross-anisotropic model to simulate the appearance of strain localisation. In addition to the classical macrokinematics, the second gradient model includes an enrichment of the continuum with microstructure effects [31, 32].

a^t	current configuration of any quantity a at a given time t	
a^*	virtual quantity a	
x_i	current coordinate	m
Ω	porous material configuration	m^3
Γ	porous material boundary	m^2
σ_{ij}	Cauchy total stress field	Pa
v_{ij}	microkinematic gradient field	
Σ_{ijk}	double stress dual of microkinematic second gradient field	$Pa \cdot m$
$\bar{t}_i$	external traction force per unit area	Pa
$\overline{T}_i$	external double force per unit area	$Pa \cdot m$
n_i	normal unit vector	
λ_{ij}	field of Lagrange multipliers	Pa
$\dot{M}_w$	water mass variation	$kg/m^3 s$
p_w	pore water pressure	Pa
$m_{w,i}$	water mass flow	$kg/m^2 s$
Q	water sink term	$kg/m^3 s$
$\bar{q}$	input water mass per unit area	$kg/m^2 s$

The momentum balance equations governing the local second gradient coupled problem in saturated conditions are the following:

$$\int_{\Omega^t} \left(\sigma_{ij}^t \frac{\partial u_i^*}{\partial x_j^t} + \Sigma_{ijk}^t \frac{\partial v_{ij}^*}{\partial x_k^t} - \lambda_{ij}^t \left(\frac{\partial u_i^*}{\partial x_j^t} - v_{ij}^* \right) \right) d\Omega^t$$
$$= \int_{\Gamma_\sigma^t} \left(\bar{t}_i u_i^* + \overline{T}_i v_{ik}^* n_k^t \right) d\Gamma^t \tag{29}$$

$$\int_{\Omega^t} \lambda_{ij}^* \left(\frac{\partial u_i^t}{\partial x_j^t} - v_{ij}^t \right) d\Omega^t = 0 \tag{30}$$

$$\int_{\Omega^t} \left(\dot{M}_w^t p_w^* - m_{w,i}^t \frac{\partial p_w^*}{\partial x_i^t} \right) d\Omega^t = \int_{\Omega^t} Q^t p_w^* d\Omega^t - \int_{\Gamma_q^t} \bar{q}^t p_w^* d\Gamma^t \tag{31}$$

The coupled finite element formulation is defined by the non-linear system of equations (29), (30) and (31). More details about the developments of these equations are available in [33], derived from the equality between internal and external virtual works. Moreover, the linearisation of these equations is also defined in [33].

The strain localisation is shown during a 2D plane strain biaxial test. The representation of the hydro-mechanical model under undrained condition is detailed in Figure 13. The considered sample has a height of 50mm and a width of 20mm, the bedding is disposed horizontally. To facilitate the localisation, a material imperfection is introduced in one element of the mesh, the cohesion is divided by 10 for this element. The sample boundaries are impervious and a constant confining pressure of 6MPa is applied. The initial water pressure is equal to 5MPa.
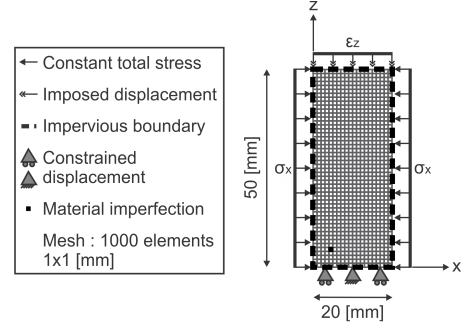

Figure 13: Numerical model used for the modelling of a plane-strain biaxial compression test.

To model the vertical compression, the vertical displacement of all nodes of the sample's upper surface is progressively increased during the test with a constant loading strain rate of $1 \times 10^{-6} \ s^{-1}$ up to 1.5 mm, which corresponds to a total vertical strain of $\epsilon_z = 0.03$. The vertical displacement of all nodes of the bottom surface is blocked and the displacement of the central node is blocked both in the vertical and horizontal direction to avoid rigid body displacement.

The biaxial compression test is performed using the orthotropic model with the parameters presented in Table 3 except $B_c = 0.05$ instead of 0.002 to slowdown the softening. The offset δ between the hardening and the softening is taken equal to 0.004 and the water compressibility is $1/\chi = 5 \cdot 10^{-10} \ \text{Pa}^{-1}$. Figure 14 presents the axial load - axial deformation curve corresponding to the simulation performed with these parameters.
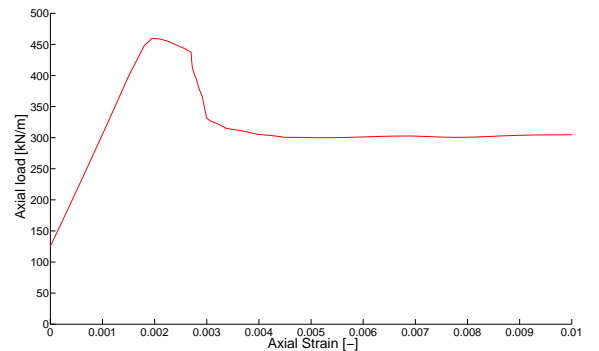

Figure 14: Orthotropic model - Biaxial test: load - strain

In order to understand the evolution of the shear band activity during the biaxial loading, different variables evolution are presented:

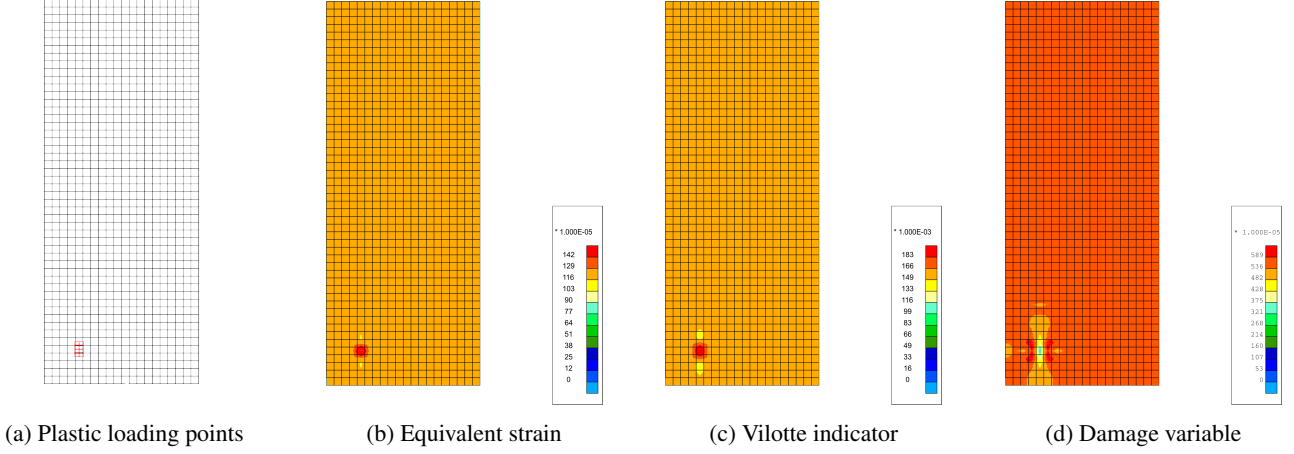- First, the plastic loading points indicate the plastic zone (red squares).

9

(a) Plastic loading points (b) Equivalent strain (c) Vilotte indicator (d) Damage variable

Figure 15: Orthotropic model - Axial deformation $1.5 \cdot 10^{-3}$.

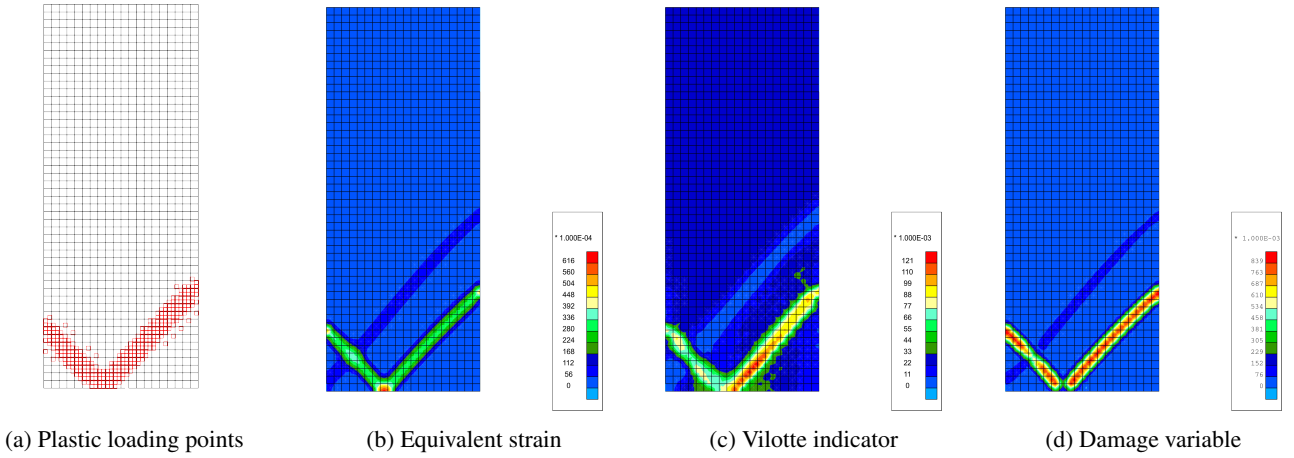(a) Plastic loading points (b) Equivalent strain (c) Vilotte indicator (d) Damage variable

Figure 16: Orthotropic model - Axial deformation $3.0 \cdot 10^{-3}$.

- Then, there is the Von Mises' equivalent deviatoric total strain defined by

$$\hat{\epsilon}_{eq} = \sqrt{\frac{2}{3} \, \hat{\epsilon}_{ij} \, \hat{\epsilon}_{ij}} \qquad (32)$$

where $\hat{\epsilon}_{ij} = \epsilon_{ij} - \frac{\epsilon_{kk}}{3} \, \delta_{ij}$ is the deviatoric total strain field calculated from the total strain tensor ϵ_{ij}.

- Finally, the deviatoric strain increment, also named Vilotte indicator, represents the band activity and is defined by:

$$\kappa = \frac{\dot{\hat{\epsilon}}_{eq} \, dt}{\int \dot{\hat{\epsilon}}_{eq} \, dt} \qquad (33)$$

Figures 15 and 16 present the evolutions of these interesting variables during the biaxial test. Figure 15 corresponds approximately to the beginning of the localisation. It happens before the peak from Figure 14 and it is initiated where the defect has been placed. Figure 16 is given after the peak and a shear band is clearly formed. The distribution of the damage variable shows that highest values are in the shear band, where the maximum elastic strain has been reached.

In the next section, the excavation of a tunnel is simulated with the same model and material parameters.

7. Gallery excavation simulation

The modelling of a tunnel drilling in rock is performed in two-dimensional plane-strain state. The bedding is disposed horizontally and the parameters are the same that ones used for the biaxial test. The stress field is also anisotropic, the vertical stress is 40MPa, the horizontal stresses are 25MPa in the two directions and the water pressure is 5MPa. In fact, *in situ* stresses have been boosted in this case study to try to provoke localisation. The pore pressure used is however conceivable in a mountainous environment.

Concerning the boundary conditions, the initial pore water pressure and stresses are imposed constant at the mesh external boundaries. On the wall of the tunnel, the water pressures are progressively decreased to atmospheric pressure. Finally, the normal displacements and the water flow are blocked to zero along the symmetry axes (impervious axes) in order to establish the symmetry.

The excavation of the tunnel is performed with the convergence-confinement method which is an approximation
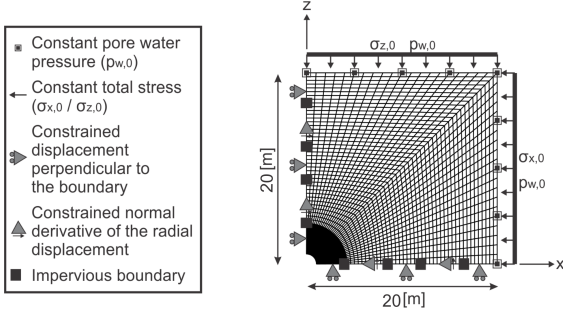
10

Figure 17: Numerical model used for the modelling of a tunnel excavation.

method for tunnelling that allows transforming a whole three dimensional study of tunnel excavation into a two dimensional study in plane-strain state, based on an identical tunnel convergence assumption. The effect of the excavation front progress is taken into account by applying a fictive pressure σ_r^Γ on the tunnel wall that depends on the proximity of the excavation front to the studied tunnel section, as detailed in Figure 18. A deconfinement rate ζ ranging from 0 to 1 is defined by:

$$\sigma_r^\Gamma = (1 - \zeta)\,\sigma_{r,0} \qquad (34)$$

where $\sigma_{r,0}$ is the initial pressure on the tunnel wall that corresponds to the initial stress in the material.
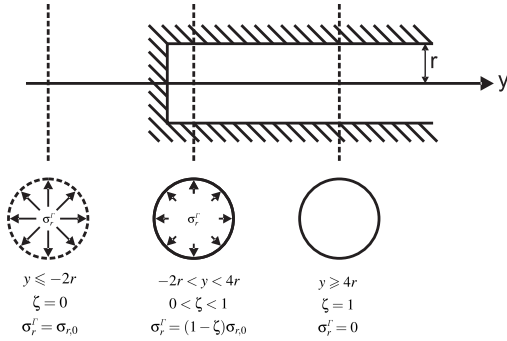

Figure 18: Deconfinement rate during tunnel excavation.

For the simulation performed, the excavation phase lasts 5 days. ζ does not reach totally 1 because a residual confinement pressure of $100kPa$ is maintained at the wall of the tunnel. The diameter of the tunnel is 4.6m.

Figure 19 present the plastic loading points, the equivalent strain and the Vilotte indicator at the end of the excavation. The graphic zone is restricted to 5 over 5 m around the tunnel. In fact, because of its high strength parameters, Opalinus clay does not localise during the excavation as easily as for the biaxial test. However, the Vilotte indicator, which is an incremented variable, shows that shear banding activity is occurring. The shear bands are surrounded in Figure 19c at the end of the excavation. These bands appear horizontally. It is not surprising because the initial stresses are maximum in this direction and the cohesion is also lower than perpendicular to the bedding plane.
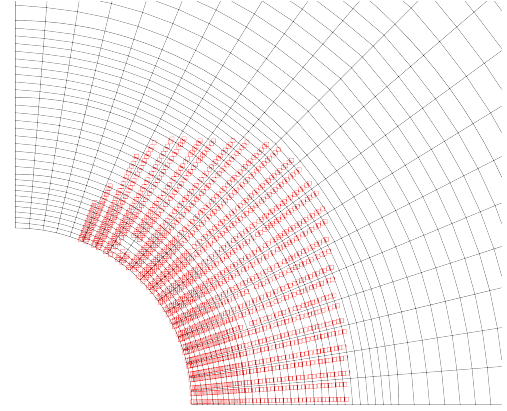
(a) Plastic loading points
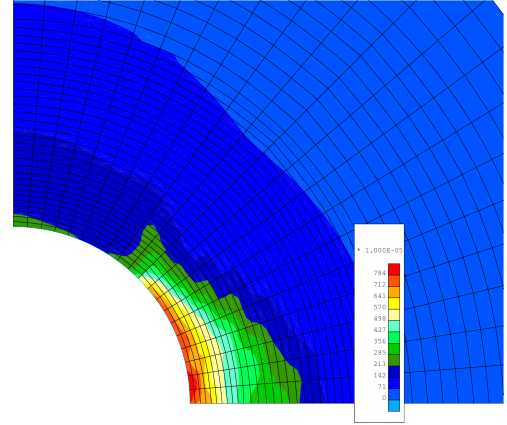
(b) Equivalent strain
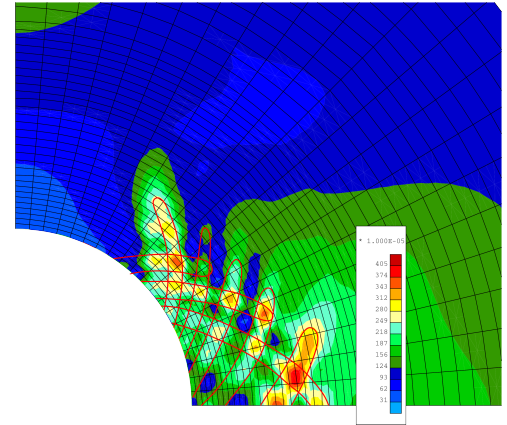
(c) Vilotte indicator

Figure 19: tunnel excavation after 5 days (end of excavation).

8. Conclusion

The constitutive model presented includes anisotropy of the elastic and plastic behaviours. The first version of the model allows fitting the deviatoric stress evolutions obtained experimentally by Jahns [1] during triaxial tests. The objective was to fit different tests simultaneously with the same set of parameters and not to fit them all individually. Indeed, a unique set of parameters which is representative of the material is required to simulate the excavation of a tunnel. However, the first version

11

of the model requires the definition of different Young moduli to fit data from different confinement pressures. Moreover, the model does not allow fitting properly the pore pressure evolutions. Thence, a variable dilatancy angle was introduced to best fit the pore pressure evolutions and the model has been improved to take into account the variation of Young moduli experimentally observed with different confinement pressures. To do so, a hyperbolic variation of the dilatancy angle with plastic strains and a linear evolution of the Young modulus with the mean pressure were introduced. Moreover, a variation of the elastic properties with damage was also considered. In fact, because the modifications on elastic properties have antagonistic effects, they do not modify the fitting so much but tend to a unique set of parameters. The fitting of pore pressures is really improved by the variable dilatancy angle; it can be noticed more evidently with all the simulations performed isotropically (see Appendix A). Finally, the improved cross-anisotropic model was used together with a coupled local second gradient model. First, the ability of the Lagamine code to reproduce the shear strain localisation was demonstrated during a 2D plane strain biaxial test. This model was finally applied to simulate the excavation of a tunnel.

Acknowledgements

References

[1] E. Jahns, "Geomechanical laboratory tests on opalinus clay cores from the bore hole schlattingen sla-1," *Nagra Work Report NAB*, pp. 13–18, 2013.

[2] M. Schneider, A. Froggatt, *et al.*, "World nuclear industry status report 2015," 2015.

[3] NEA, "Moving forward with geological disposal of radioactive waste, a collective statement by the nea radioactive waste management commitee (rwmc)," tech. rep., OECD-Nuclear Energy Agency, Paris, 2008.

[4] W. R. Alexander and L. McKinley, *Deep geological disposal of radioactive waste*, vol. 9. Elsevier, 2011.

[5] D. ANDRA, "Les recherches de l'andra sur le stockage géologique des déchets radioactifs à haute activité et à vie longue, résultats et perspectives, ed," *Cl Rapports*, vol. 265, 2005.

[6] ONDRAF/NIRAS, "Technical overview of the safir 2 report: Safety assessment and feasibility interim report 2," tech. rep., 2001.

[7] C. Martin and G. Lanyon, "Measurement of in-situ stress in weak rocks at mont terri rock laboratory, switzerland," *International Journal of Rock Mechanics and Mining Sciences*, vol. 40, no. 7, pp. 1077–1088, 2003.

[8] P. Bossart, T. Trick, P. M. Meier, and J.-C. Mayor, "Structural and hydrogeological characterisation of the excavation-disturbed zone in the opalinus clay (mont terri project, switzerland)," *Applied clay science*, vol. 26, no. 1, pp. 429–448, 2004.

[9] H. Bock, "Ra experiment: rock mechanics analysis and synthesis: conceptual model of the opalinus clay," *Mont Terri Techn. Rep*, vol. 3, 2001.

[10] Y. Wileveau, "THM behaviour of host rock (HE-D) experiment: Progress report," tech. rep., Part 1, Technical Report TR 2005-03. Mont Terri Project, 2005.

[11] A. Gens, J. Vaunat, B. Garitte, and Y. Wileveau, "In situ behaviour of a stiff layered clay subject to thermal loading: observations and interpretation," *Géotechnique*, vol. 57, no. 2, pp. 207–228, 2007.

[12] A. Lisjak, B. S. Tatone, G. Grasselli, and T. Vietor, "Numerical modelling of the anisotropic mechanical behaviour of opalinus clay at the laboratory-scale using fem/dem," *Rock mechanics and rock engineering*, vol. 47, no. 1, pp. 187–206, 2014.

[13] B. Pardoen, D. Seyedi, and F. Collin, "Shear banding modelling in cross-anisotropic rocks," *International Journal of Solids and Structures*, vol. 72, pp. 63–87, 2015.

[14] A. Skempton, "The pore-pressure coefficients a and b," *Geotechnique*, vol. 4, no. 4, pp. 143–147, 1954.

[15] S. Levasseur, J.-P. Radu, and F. Collin, "Analysis of core samples from Schlattingen SLA-1 borehole for geomechanical characterization of opalinus clay through constitutive modelling approach by Université de Liège," *Nagra Arbeitsbericht. NAB 14-094*, 2014.

[16] O. Coussy, *Poromechanics*. John Wiley & Sons, 2004.

[17] H. Darcy, *Les fontaines publiques de la ville de Dijon*. Librairie des Corps Impriaux des Ponts et Chausses et des Mines, 1856.

[18] S. G. Lekhnitskii, *Theory of Elasticity of an Anisotropic Elastic Body*. San Francisco: Holden-Day, 1963.

[19] B. Amadei, *Rock anisotropy and the theory of stress measurements*, vol. 2. New York: Springer-Verlag, 1983. Lecture Notes in Engineering Series.

[20] D. Drucker and W. Prager, "Solid mechanics and plastic analysis for limit design," *Quarterly of Applied Mathematics*, vol. 20, no. 2, pp. 157–165, 1952.

[21] J. D. Barnichon, "Finite element modelling in structural and petroleum geology (PhD Thesis)," 1998.

[22] G. Duveau, J. Shao, and J. Henry, "Assessment of some failure criteria for strongly anisotropic geomaterials," *Mechanics of Cohesive-frictional Materials*, vol. 3, no. 1, pp. 1–26, 1998.

[23] B. François, V. Labiouse, A. Dizier, F. Marinelli, R. Charlier, and F. Collin, "Hollow cylinder tests on boom clay: Modelling of strain localization in the anisotropic excavation damaged zone," *Rock mechanics and rock engineering*, vol. 47, no. 1, pp. 71–86, 2014.

[24] S. Pietruszczak and Z. Mroz, "Formulation of anisotropic failure criteria incorporating a microstructure tensor," *Computers and Geotechnics*, vol. 26, no. 2, pp. 105–112, 2000.

[25] P. V. Lade, "Modeling failure in cross-anisotropic frictional materials," *International Journal of Solids and Structures*, vol. 44, no. 16, pp. 5146–5162, 2007.

[26] R. Charlier, *Approche unifiée de quelques problèmes non linéaires de mécanique des milieux continus par éléments finis*. PhD thesis, Université de Liège, 1987.

[27] F. Collin, *Couplages thermo-hydro-mécaniques dans les sols et les roches tendres partiellement saturés*. PhD thesis, Université de Liège, 2003.

[28] L. Chen, J.-F. Shao, and H. Huang, "Coupled elastoplastic damage modeling of anisotropic rocks," *Computers and Geotechnics*, vol. 37, no. 1, pp. 187–194, 2010.

[29] J.-F. Shao, Y. Jia, D. Kondo, and A.-S. Chiarelli, "A coupled elastoplastic damage model for semi-brittle materials and extension to unsaturated conditions," *Mechanics of materials*, vol. 38, no. 3, pp. 218–232, 2006.

[30] K. El Moustapha, "Identification of an enriched constitutive law for geomaterials in the presence of a strain localisation," 2014.

[31] R. Chambon, D. Caillerie, and N. El Hassan, "One-dimensional localisation studied with a second grade model," *European Journal of Mechanics-A/Solids*, vol. 17, no. 4, pp. 637–656, 1998.

[32] R. Chambon, D. Caillerie, and T. Matsuchima, "Plastic continuum with microstructure, local second gradient theories for geomaterials: localization studies," *International Journal of Solids and Structures*, vol. 38, no. 46, pp. 8503–8527, 2001.

[33] F. Collin, R. Chambon, and R. Charlier, "A finite element method for poro mechanical modelling of geotechnical problems using local second gradient models," *International journal for numerical methods in engineering*, vol. 65, no. 11, pp. 1749–1772, 2006.

Appendix A. Isotropic simulations

P-samples (0°)

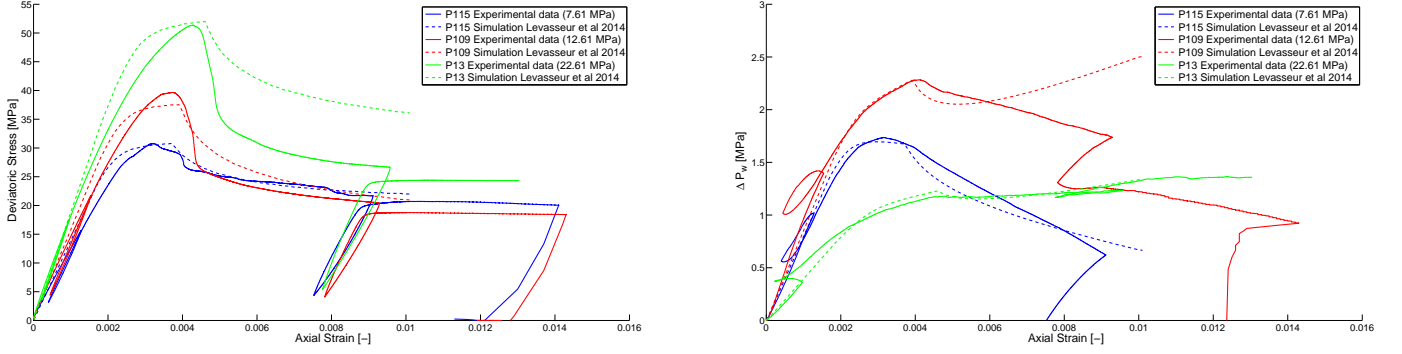Figure A1: P-samples: Deviatoric Stress and Pore Pressure evolutions

	E	ν	ψ	ϕ'_0	ϕ'_f	B_p	c'_0	c'_f	B_c	δ	$\dfrac{1}{\chi}$
P115	13.8	0.46	0.1°	20.0°	29.8°	0.0001	6.4	2.5	0.002	0.0015	2.5E-10
P109	15.4	0.15	-4.0°	20.0°	29.8°	0.0001	6.4	1.0E-05	0.002	0.0015	4.25E-09
P13	18.7	0.22	-3.0°	20.0°	29.8°	0.0001	6.4	1.0E-05	0.002	0.0018	8.0E-09

Table A1: Parameters for P simulations; E [GPa], c' [MPa], $\frac{1}{\chi}$ [Pa^{-1}].
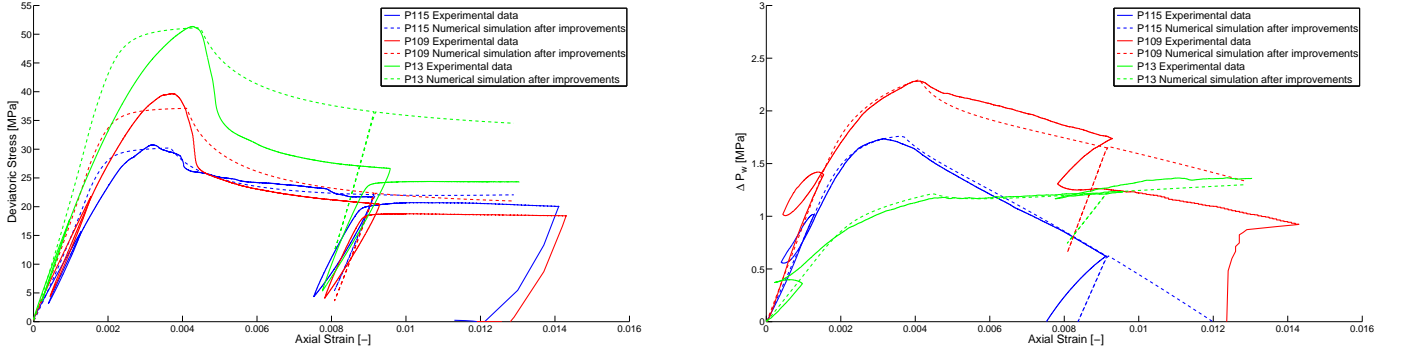

Figure A2: P-samples: Deviatoric Stress and Pore Pressure evolutions after model improvements

	E_0	α_E	ν	ψ_0	ψ_f	B_d	ϕ'_0	ϕ'_f	B_p	c'_0	c'_f	B_c	δ
P115	10.41	0.5516	0.46	-0.45°	0.475°	0.002	20.0°	29.8°	0.0001	6.4	2.5	0.002	0.0015
P109	10.41	0.5516	0.15	-8.5°	3.5°	0.002	20.0°	29.8°	0.0001	6.4	1.0E-05	0.002	0.0015
P13	10.41	0.5516	0.22	-6°	0°	0.002	20.0°	29.8°	0.0001	6.4	1.0E-05	0.002	0.0018

Table A2: Parameters for P simulations after model improvements; E_0 [GPa], α_E for σ_M [MPa], c' [MPa].
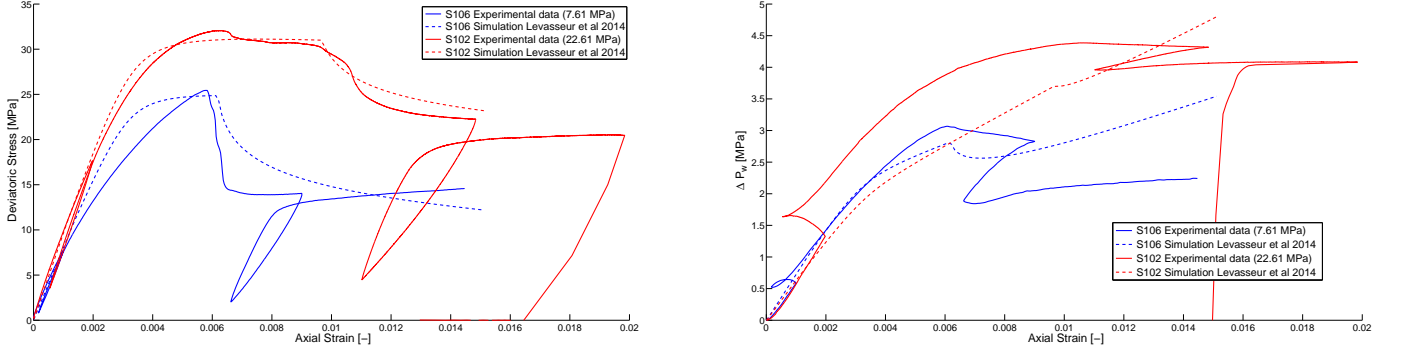
S-samples (90°)

Figure A3: S-samples: Deviatoric Stress and Pore Pressure evolutions

	E	ν	ψ	ϕ'_0	ϕ'_f	B_p	c'_0	c'_f	B_c	δ	$\frac{1}{\chi}$
S106	7.8	0.30	-3.0°	0.0°	29.0°	0.0001	5.4	1.0	0.002	0.0030	2.5E-09
S102	9.5	0.34	-4.0°	0.0°	20.5°	0.0001	5.4	2.0	0.002	0.0062	2.5E-09

Table A3: Parameters for S simulations; E [GPa], c' [MPa], $\frac{1}{\chi}$ [Pa^{-1}].
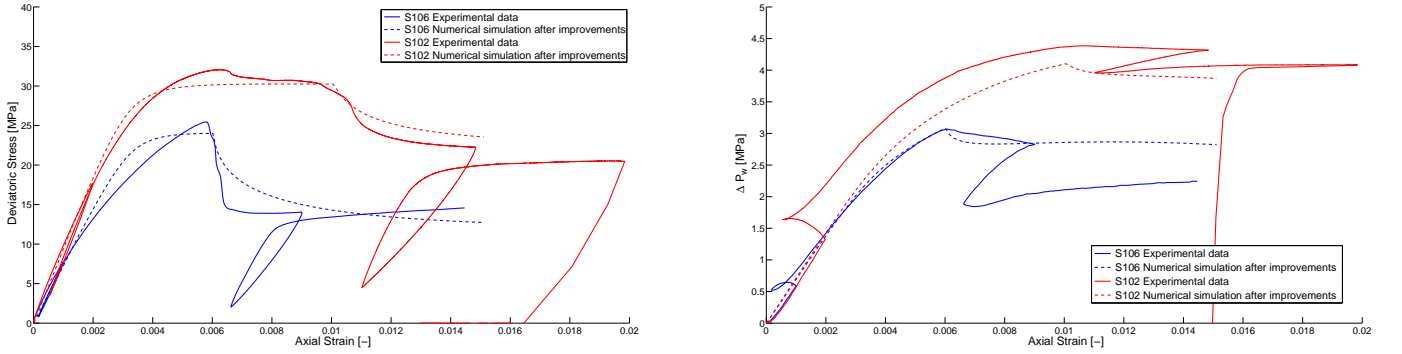

Figure A4: S-samples: Deviatoric Stress and Pore Pressure evolutions after model improvements

	E_0	α_E	ν	ψ_0	ψ_f	B_d	ϕ'_0	ϕ'_f	B_p	c'_0	c'_f	B_c	δ
S106	5.87	0.1852	0.30	-7.5°	3°	0.005	0.0°	29.0°	0.0001	5.4	1.0	0.002	0.0030
S102	5.87	0.1852	0.34	-8°	2.5°	0.004	0.0°	20.5°	0.0001	5.4	2.0	0.002	0.0062

Table A4: Parameters for S simulations after model improvements; E_0 [GPa], α_E for σ_M MPa, c' [MPa].
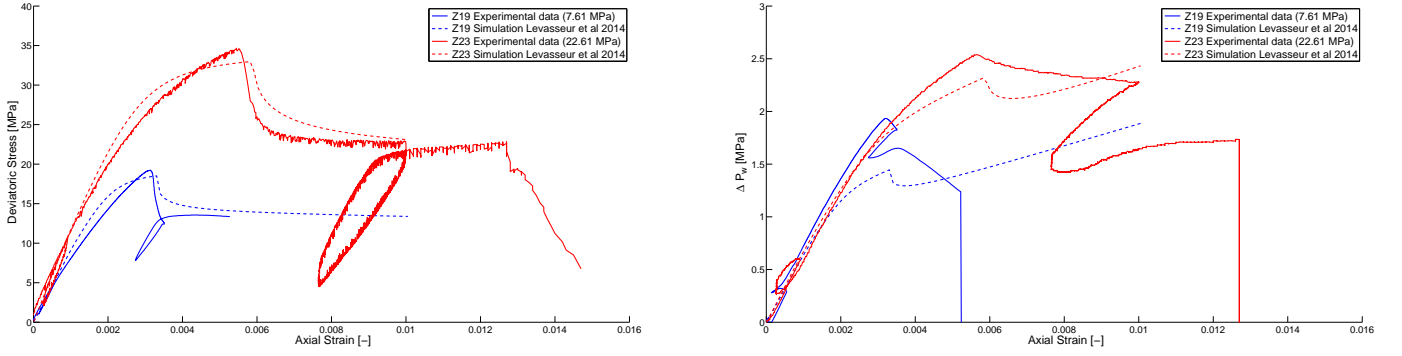
Z-samples (45°)

Figure A5: Z-samples: Deviatoric Stress and Pore Pressure evolutions

	E	ν	ψ	ϕ'_0	ϕ'_f	B_p	c'_0	c'_f	B_c	δ	$\frac{1}{\chi}$
Z19	9.1	0.40	-1.0°	0.0°	23.1°	0.0001	4.5	2.5	0.0004	0.0013	1.5E-09
Z23	11.7	0.10	-5.0°	0.0°	23.1°	0.00015	4.5	0.1	0.001	0.0030	6.0E-09

Table A5: Parameters for Z simulations; E [GPa], c' [MPa], $\frac{1}{\chi}$ [Pa^{-1}].
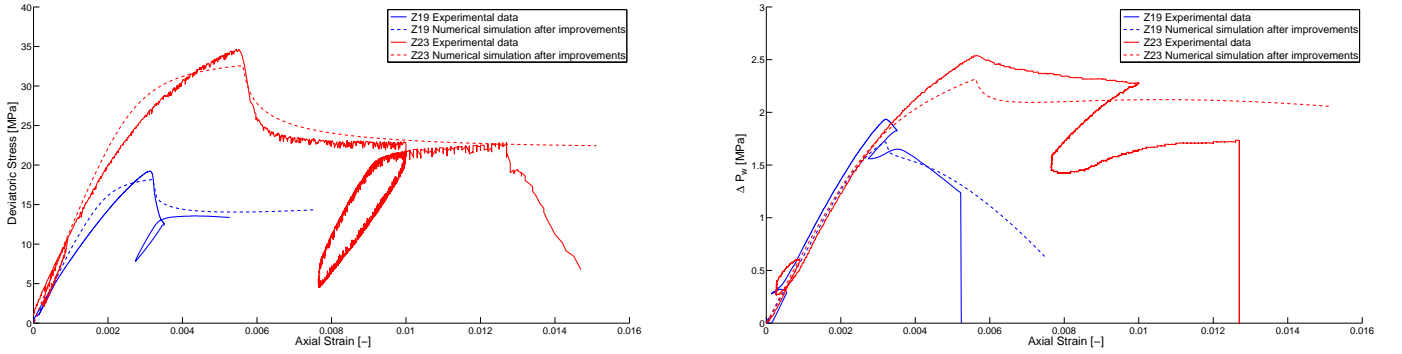

Figure A6: Z-samples: Deviatoric Stress and Pore Pressure evolutions after model improvements

	E_0	α_E	ν	ψ_0	ψ_f	B_d	ϕ'_0	ϕ'_f	B_p	c'_0	c'_f	B_c	δ
Z19	7.89	0.2123	0.40	-6.5°	6.5°	0.002	0.0°	23.1°	0.0001	4.5	2.5	0.0004	0.0013
Z23	7.89	0.2123	0.10	-10 °	4°	0.004	0.0°	23.1°	0.00015	4.5	0.1	0.001	0.0030

Table A6: Parameters for Z simulations after model improvements; E_0 [GPa], α_E for σ_M MPa, c' [MPa].